

Quake-DFN, A software for Simulating Sequences of Induced Earthquakes in a Discrete Fault Network

Kyungjae Im* and Jean-Philippe Avouac

4 *Geology and Planetary Science Division, California Institute of Technology, Pasadena, CA*

5 91125, United States

6 *Correspondence to: kjim@caltech.edu

8 Abstract

We present an earthquake simulator, Quake-DFN, which allows simulating sequences of earthquakes in a 3-D Discrete Fault Network governed by rate and state friction. The simulator is quasi-dynamic, with inertial effects being approximated by radiation damping and a lumped mass. The lumped mass term allows accounting for inertial overshoot and, in addition, makes the computation more effective. Quake-DFN is compared against three publicly available simulation results: (i) the rupture of planar fault with uniform prestress (SEAS BP5-QD), (ii) the propagation of a rupture across a step-over separating two parallel planar faults (RSQSim and FaultMod), and (iii) a branch fault system with a secondary fault splaying from a main fault (FaultMod). Examples of injection-induced earthquake simulations are shown for three different fault geometries: (i) a planar fault with a wide range of initial stresses, (ii) a branching fault system with varying fault angles and principal stress orientations, and (iii) a fault network similar to the one that was activated during the 2011 Prague earthquake sequence in Oklahoma. The simulations produce realistic earthquake sequences. The time and magnitude of the induced

22 earthquakes observed in these simulations depend on the difference between the initial friction
23 and the residual friction $\mu_i - \mu_f$, the value of which quantifies the potential for run-away ruptures
24 (ruptures that can extend beyond the zone of stress perturbation due to the injection). The
25 discrete fault simulations show that our simulator correctly accounts for the effect of fault
26 geometry and regional stress tensor orientation and shape. These examples show that Quake-
27 DFN can be used to simulate earthquake sequences, most importantly magnitudes, possibly
28 induced or triggered by a fluid injection near a known fault system.

29

30 **Key points**

31 1. Quake-DFN is an efficient earthquake simulator applicable to complex discrete fault systems
32 2. Three comparison studies are conducted against publicly available simulation results
33 3. Induced earthquake simulations show realistic earthquake sequences corresponding to local
34 stress fields

35

36 **1. Introduction**

37 Much progress has been made recently in stress-based induced earthquake forecasting
38 both at the conceptual level and in the modeling of real case examples (e.g., Segall and Lu, 2015;
39 Bourne and Oates., 2017; Galis et al., 2017; McGarr, 2015; Goebel and Brodsky, 2018; Norbeck
40 and Rubinstein, 2018; Zhai et al., 2020; Hager et al., 2021; Wang and Dunham, 2022; Candela et
41 al., 2022; Acosta et al., 2023). The use of stress-based earthquake simulations to forecast induced
42 earthquakes, which account for known faults, remains, however, very challenging. Well-
43 established methods exist to simulate individual dynamic rupture events on fault systems with
44 complex geometries (e.g., Harris et al., 2018) or to simulate repeating ruptures on faults with
45 planar geometries (e.g., Erickson et al., 2020; Jiang et al., 2022). Combining the two capabilities
46 is a computational challenge: resolving the effect of non-planar fault geometries and the different
47 phases of the earthquake cycle (the successive phases of nucleation, growth, and arrest of seismic
48 ruptures).

49 There is, therefore, a need for computationally efficient earthquake simulators able to
50 simulate earthquake sequences with realistic fault geometries and loading. This need has
51 motivated the development of RSQSim (Richards-Dinger and Dietrich, 2012). This simulator
52 assumes that fault slip is governed by rate and state friction, a phenomenological friction law
53 derived from laboratory experiments that allow simulation of the healing process during the
54 interseismic period as well as the nucleation process and weakening (friction drop) during slip
55 events. It allows the production of repeated ruptures on the same fault patch, accounting for
56 effective stress changes induced by fluid injections (Dieterich et al., 2015). RSQSim has been
57 shown to produce synthetic catalogs with realistic statistical properties (Shaw et al., 2018). The
58 dynamics of seismic ruptures are, however, highly simplified by making use of quasi-dynamic

59 approximation with some additional kinematic prescriptions. The recently released simulator
60 MCQSim (Zielke and Mai, 2023) adopted an alternative approach to represent dynamic effects
61 during seismic ruptures. It assumes a linear decrease of friction with fault slip, a
62 phenomenological law that can produce realistic seismic ruptures (e.g., Olsen et al., 1997). This
63 simulator produces realistic seismic ruptures, but the representation of healing and nucleation is
64 simplified (not derived from solving the equations describing fault dynamics).

65 Here, we present an earthquake simulator, Quake-DFN, which is open-source and allows
66 computationally efficient simulations of sequences of induced earthquakes on a Discrete Fault
67 Network. Our intent is to produce realistic sequences of induced earthquakes consistent with
68 empirical statistical properties of earthquakes. Like RSQSim, our simulator assumes faults
69 governed by rate and state friction embedded in a 3-D half-space, driven by stress change that
70 can result from tectonics or from human activities such as the injection or extraction of fluids
71 from the sub-surface. We opt for a simplified representation of dynamic effects by adopting a
72 quasi-dynamic approximation, but our formulation allows for inertial overshoot. This
73 formulation is identical to the 2D discrete fault network simulator presented in Im and Avouac
74 (2023), which was found to successfully reproduce the natural characteristics of earthquake
75 sequences (Omori law, inverse Omori law, Gutenberg-Richter law). The representation of fault
76 friction and the coupled processes involved in induced seismicity is oversimplified. In particular,
77 we ignore that deformation affects fluid transport properties (e.g., Viesca and Garagash, 2018;
78 Im et al., 2018; Cappa et al., 2022), but we believe that this simulator will be a useful tool to
79 improve further the understanding of induced earthquakes and the management of the seismic
80 hazard associated to CO₂ subsurface storage, geothermal energy production or wastewater

81 disposal (e.g., Ellsworth, 2013; Candela et al., 2018; Zoback and Gorelick, 2012; Lee et al.,
82 2019).

83 Hereafter, we first describe the Quake-DFN simulation method and conduct comparison
84 studies against publicly available simulation results. To illustrate the capabilities of the
85 simulator, we describe sets of simulations with increasingly complex fault geometries. We start
86 with a simple case of an injection of fluids in a pre-existing planar fault, a case also treated in
87 several previous theoretical or numerical studies (e.g., Dieterich et al., 2015; Larochelle et al.,
88 2019; Wang and Dunham, 2022; Garagash and Germanovich, 2012; Bhattacharya and Viesca,
89 2019; Saez and Lecampion, 2023). We next consider the case of branching faults in the simple
90 case of one single branch. We vary the orientation of the regional stresses and the angle between
91 the fault branch and the main fault. Finally, we consider the case of the fault system activated
92 during the 2011 Prague earthquake in Oklahoma (Keranen et al., 2013; Sumy et al., 2014). We
93 consider only the case of strike-slip faults here, but the simulator can apply to dip-slip faults.

94

95 **2. Simulation Method**

96 *2.1 Simulation of fault slip with rate and state friction*

97 Simulations of earthquake ruptures on finite-size faults governed by rate-and-state
98 friction can yield realistic simulations of fluid-induced ruptures (e.g., Dieterich et al., 2015;
99 Cappa et al., 2019; Larochelle et al., 2021; Hager et al., 2021; Wang and Dunham, 2022).
100 Simulations based on rate and state friction are, however, computationally expensive and often
101 associated with numerical instability. Stringent simplifications are therefore made in such
102 simulations. Most assume a single planar fault with constant normal stress, neglecting off-fault

103 deformation and the coupling between deformation and hydraulic properties (Dieterich et al.,
104 2015; Cappa et al., 2019; Larochelle et al., 2021). Even with these simplifications, simulating a
105 sequence of earthquakes on a set of interacting faults is a huge challenge. RSQSim allows
106 simulating sequences of earthquakes on a discrete set of faults by considering different stages
107 (called ‘states’ in the RSQSim literature; we use ‘stages’ instead to avoid confusion) to solve the
108 governing equations (Dieterich et al., 2015; Richard-Dinger and Dieterich, 2012). The faults are
109 discretized in planar cells and have prescribed rake. In the period between rupture events,
110 analytical approximations for non-interacting faults are used to solve for slip in stages 0 (healing)
111 and 1 (nucleation). The nucleation process occurs within one cell, and the numerical scheme is,
112 therefore, inherently discrete. During a rupture event (stage 2), the slip rate is prescribed and
113 constant based on some chosen stress drop ($V^{EQ} = 2\beta\Delta\tau/G$, where β , $\Delta\tau$, and G are the shear wave
114 speed, stress drop, and shear modulus, respectively). The rupture velocity is then a consequence
115 of this relationship.

116 In Quake-DFN, each fault is also discretized into rectangular planar cells, with a
117 prescribed rake, in a 3D elastic half-space with quasi-static stress transfer. The main differences
118 with RSQSim are that (1) Quake-DFN does not involve stage-based approximations nor
119 kinematic prescriptions (the same set of governing equations is solved at all times), (2) the
120 inherently discrete scheme is not needed (faults interact all the time and the cell size can be
121 smaller than the nucleation size), and (3) inertial effects are represented with a lumped mass term
122 (Im and Avouac, 2021a) in addition to the radiation damping term, introduced by Rice (1993),
123 which is commonly used in quasi-dynamic simulations.

124 With these assumptions, the momentum balance equation at i^{th} boundary element yields

125
$$M_i \ddot{\delta}_i = \sum_j k_{ij}^\tau (\delta_{0j} - \delta_j) - \mu_i (\sigma'_{0i} + \sum_j k_{ij}^\sigma \delta_j + \sigma'^E_i) - \frac{G}{2\beta} \dot{\delta}_i + \tau_i^E, \quad (1)$$

126 where δ_i is fault slip of element i , the over-dot denotes time derivative, M_i is the lumped mass per
 127 unit contact area for each element, δ_{0j} is the initial displacement of element j , σ'_{0i} is the initial
 128 effective normal stress of element i , G is shear modulus, β is shear wave speed, and k_{ij} is a
 129 stiffness matrix that defines the elastic stress change imparted on element i due to slip of element
 130 j (k^τ and k^σ represent shear and normal stiffness matrix, respectively). The stiffness matrices are
 131 calculated by assuming quasistatic stress transfer (Okada, 1992). The τ^E and σ'^E are shear and
 132 effective normal stress changes driven by external stress, such as tectonic loading or poro-elastic
 133 stress change. To simplify notations, $V (= \dot{\delta})$ denotes fault slip velocity hereafter.

134 Faults are governed by rate and state friction (Dieterich, 1979; Marone, 1998)

135
$$\mu = \mu_0 + a \log\left(\frac{V}{V_0}\right) + b \log\left(\frac{V_0 \theta}{D_c}\right) \quad (2)$$

136 and the aging law with the normal stress dependent evolution (Linker and Dieterich, 1992)

137
$$\frac{d\theta}{dt} = 1 - \frac{V\theta}{D_c} - \alpha \frac{\theta \dot{\sigma}}{b\sigma}, \quad (3)$$

138 where V is slip rate, θ is the state variable, μ_0 is the friction coefficient at the reference velocity
 139 V_0 (chosen arbitrarily, here we choose a value of 10^{-9} m/s), D_c is a critical slip distance, and a and
 140 b are empirical constants for the magnitude of direct and evolution effects, respectively. The
 141 Linker-Dieterich term, α , describes the effect of the normal stress rate on the state evolution. It
 142 implies that the coefficient of friction is sensitive to the normal stress evolution. It, therefore,
 143 comes into play when there is a significant change in normal stress (Alghannam and Juanes,
 144 2020; Kroll et al., 2023). The effect of pore pressure on fault slip is, however, primarily due to
 145 the impact on the effective stress, which occurs even if α is set to zero. For simplicity, we set $\alpha =$

146 0 for the simulations presented in the main text simulations. However, the influence of this term
147 is presented in additional simulations and discussed in the supplementary material. We
148 conducted multiple simulations with varied α values and found that this term plays an important
149 role when α is sufficiently large ($\alpha > 0.12$). The state variable θ has a unit of time (s) and allows
150 for frictional healing. Given $\alpha = 0$ in the main text simulations, the healing rate is maximum
151 when the fault is stationary ($V=0$). In that case, θ increases as 1s/s.

152 The radiation damping term, $\delta_i G / 2\beta$ (Rice 1993) accounts approximately for the loss of
153 energy due to seismic wave radiations. The lumped mass ($M_i \ddot{\delta}_i$) allows for inertial overshoot and
154 friction-induced vibrations (Im and Avouac 2021a). Overshoot appears in fully dynamic
155 simulations and results in static slip larger than the slip that would have occurred in the absence
156 of inertia (e.g., Madariaga, 1976; Thomas et al., 2014). An overshoot factor, as defined by Ben-
157 Zion (1996), is also included in RSQSim (Richards-Dinger and Dieterich, 2012) or MCQSim
158 (Zielke and Mai, 2023). The lumped mass per unit area M represents the inertia of the mass
159 involved in the rupture process. If the rupture size is fixed and assumed equal to the fault size, M
160 can be defined as

$$161 M = \frac{\rho L}{(1-\nu)\pi^2}, \quad (4)$$

162 where L is the length scale of the rupture size, ρ is rock density, and ν is Poisson's ratio.
163 Conversely, if the rupture size is not fixed, L may be approximated by the expected rupture scale
164 in the simulations. In this work, we assumed a constant M value of 10^6 kg/m^2 for the planar fault
165 simulation and 10^7 kg/m^2 for the other simulations. If $M = 0$, equation 1 is simplified to the
166 widely used quasi-dynamic approximation (Rice, 1993; Lapusta et al., 2000; Erickson et al.,
167 2020). We show later that our simulation results become equivalent to those obtained in quasi-

168 dynamic simulations if M is sufficiently small. The simulation uses the method of Im et al.
169 (2017), which allows larger timesteps during the rupture phase by utilizing the lumped mass
170 term. Therefore, in Quake-DFN, the lumped mass term helps stabilize the numerical scheme and
171 accelerate numerical convergence. One needs to keep in mind that the dynamic stress transfers
172 associated with seismic waves are not resolved, so Quake-DFN cannot estimate the rupture
173 velocity, but it can correctly predict slip distributions as happens in quasi-dynamic simulations
174 (Thomas et al., 2014). Our simulator has no restriction on grid size. But to avoid an inherently
175 discrete scheme, one may choose a grid size smaller than the critical length scale (Rice, 1993)

176
$$L_c = \frac{\gamma G D_c}{\sigma(b-a)}, \quad (5)$$

177 where γ is a factor close to unity, which depends on the shape of the grid cells.

178 Three different fault geometries are considered in the simulations presented in this study:
179 (1) a single planar fault (figure 1a), (2) two interacting discrete faults (figure 1b), and (3) a
180 complex fault network adopted from studies of the 2012 Prague earthquake sequence in
181 Oklahoma (Keranen et al., 2013; Sumy et al., 2014) (figure 1c). In the planar fault simulations,
182 we investigate the influence of the initial conditions of V_i and θ_i . In the other two cases, the
183 initial friction μ_i is calculated from the applied stress field, θ_i is assumed in the range of years ~
184 tens of thousands years, and V_i is determined accordingly based on equation 2.

185 Given the bulk medium properties (M, G, β, k_{ij}) and the fault friction parameters (a, b, D_c ,
186 μ_0), the set of equations 1-3 can be solved for any initial conditions represented by μ_i , V_i , and θ_i .
187 The initial friction coefficient (μ_i) is determined by the local stress tensor. Hence, the only two
188 values that are typically unknown are the initial values of the velocity (V_i) and state variable (θ_i).
189 We can bracket the initial value of θ_i since its maximum value is the elapsed time from the last

190 rupture (maximum $d\theta/dt = 1$ s/s), while the V_i has no such limit. For example, in the Prague
191 earthquake simulation, we first set the initial θ_i in the range between 10^{10} and 10^{12} s (300 to 30k
192 years), and V_i is determined correspondingly by equation 2.

193 We utilize two methods to solve equations 1-3: (i) a typical iterative method that is
194 applied to a low-velocity system and (ii) the method of Im et al. (2017), which is stable at high
195 velocity. The two solvers are automatically switched for each element based on their velocities.
196 The timestep is dependent on the maximum velocity but automatically adapts if it fails to find a
197 converged solution.

198

199 *2.2 Simulation of pore pressure diffusion and poro-elastic stress transfers*

200 The external shear and effective normal stress terms, respectively τ^E and σ^E in equation
201 1, are time-dependent and can account for tectonic loading or poro-thermo-elastic stress changes.
202 These forcing terms can be calculated from an external geomechanical model. In the simulations
203 of injection-induced seismicity presented in this study, we follow the approach of Segall and Lu
204 (2015). We calculate poroelastic stress change assuming isotropic pressure diffusion from a point
205 source of injection. The governing equation for pressure diffusion is

206
$$\frac{k}{\eta} \nabla^2 P + q = S \frac{\partial P}{\partial t}, \quad (6)$$

207 where P is pressure, k is permeability, η is viscosity, q is volumetric flow rate, and S is storage
208 coefficient. The spherical diffusion solution of equation 6 and the corresponding poro-elastic
209 stress change is given by Rudnicki (1986). The solutions are evaluated at the center of each
210 element and rotated for each fault plane and slip direction to estimate τ^E and σ^E . We use constant
211 viscosity ($\eta = 0.4 \times 10^{-3}$ Pa/s), density (1000kg/m³), and storage ($S = 2 \times 10^{-11}$; S is equivalent to

212 $k/\eta c$ in Rudnicki's solution) for all simulations. This model was chosen for simplicity. In reality,
213 the permeability would be neither homogeneous nor isotropic, and faults and fractures usually
214 have greater permeability than the rock matrices. The pressure sometimes becomes higher than
215 the initial normal stress, leading to a numerical instability. To avoid such instability, we impose a
216 minimum effective normal of 2 MPa.

217

218 **3. Comparison Studies**

219 Here, we compare our simulator to publicly available simulation results. These tests are
220 meant to show that Quake-DFN adequately simulates seismic ruptures for simple fault
221 geometries in the absence of any fluid injection. We conducted simulations of three standard
222 problems: (i) the rupture of a planar fault with uniform prestress, (ii) the propagation of a rupture
223 across a step-over separating two parallel planar faults, and (iii) a branch fault system with a
224 secondary fault splaying from a main fault.

225 *3.1 Comparison Study 1- Planar fault (SEAS BP5-QD benchmark test)*

226 We tested our simulator in the case of a simple planar fault geometry against the
227 benchmark problem – BP5QD (quasi-dynamic planar fault rupture simulation) from the
228 Community Code Verification Exercise for Simulating Sequences of Earthquakes and Aseismic
229 of the Southern California Earthquake Center (Erickson et al., 2020; Jiang et al., 2022). This test
230 allows checking that our simulator is consistent with the widely used quasi-dynamic formulation
231 when the lumped mass term is small. Given the average length scale of rupture zone size of the
232 BP5QD problem is 36km (60km \times 12km), according to equation 4 with $\rho = 2670\text{kg}$, the lumped
233 mass $M = \sim 10^7 \text{ kg/m}^2$. We conducted four simulations with $M = 10^5, 10^6, 10^7$, and 10^8 kg/m^2 .

234 This sensitivity test is to investigate the influence of the M on the inertial overshoot. As M
235 decreases, the simulation result should converge to benchmark results since equation 1
236 approaches the widely used quasi-dynamic formulation.

237 Our simulation compares well with the SEAS benchmark test (Figure 2). The simulation
238 with the nominal mass (given by equation 4) shows a slightly longer recurrence time and larger
239 stress drop (blue line) than the benchmark solution (black line) due to the inertial overshoot. The
240 overshoot effect increases if we increase M (gray line). Conversely, as expected, the simulation
241 result converges to the benchmark simulation result as we reduce M . When the effect of the mass
242 is not negligible, overshoot results in a larger slip and stress drop than for a quasi-dynamic slip
243 event. As a result, the time interval between successive events is increased. This benchmark test
244 shows that our simulation results are consistent with the quasi-dynamic formulation as the
245 inertial overshoot effect vanishes.

246 *3.2 Comparison Study 2- fault step-over*

247 The second comparison test is a step-over fault system (figure 3a). It consists of two
248 parallel planar left-lateral faults where a rupture can jump from one fault to the other across a
249 compressional step-over. The two faults have the same uniform initial stress. Simulations of this
250 comparison test conducted with RSQSim and FaultMod are presented in Kroll et al. (2023).
251 These simulators solve the friction-governed motion of fault slip, but their governing equations
252 differ from our simulator. FaultMod is a fully dynamic FEM solver with slip-weakening friction.
253 RSQSim is, like Quake-DFN, a boundary element solver based on rate and state friction with
254 quasi-static stress transfer (Richards-Dinger and Dieterich 2012). Instead of using radiation
255 damping or a lumped mass, it resorts to a stage-based approximation with a constant dynamic
256 slip rate (In Kroll et al., 2023, the authors used the fault-slip rate prescribing a rupture velocity

257 equal to that predicted by FaultMod). Hence, we do not expect Quake-DFN to yield results
258 identical to those obtained with RSQSim or FaultMod by Kroll et al. (2023). In our Quake-DFN
259 simulations, we pay attention to replicating the slip distribution (or, equivalently, the stress drop)
260 as our aim is primarily to correctly predict the final magnitude. The rupture velocity and fault
261 slip rates are probably not physical during seismic slip, given the way dynamic effects are
262 approximated. However, the results obtained with FaultMod, RSQSim, and Quake-DFN should
263 be comparable with regard to the slip distributions. To replicate the problem as described in
264 Kroll et al. (2023), the normal stress is set uniformly 60 MPa on both faults. We impose friction
265 parameters ($a=0.01$, $b=0.012$, $D_c=10\mu\text{m}$) and initial conditions ($\theta_i = 2.6 \times 10^{10}$, and $V_i = 2.17 \times 10^{-13}$)
266 to simulate the friction drop described in Kroll et al. (2023) (initial friction 0.49 dropping to
267 ~ 0.38).

268 Our simulation result is indeed comparable to the compared simulations. The final slip
269 distribution is similar in all simulators (figure 3 colormap), except some horizontal spikes appear
270 in RSQSim (figure 3f,g). Conversely, rupture propagation is somewhat different between the
271 solvers. In our simulation, the rupture speed is slower, as has been found in previous studies
272 comparing quasi-dynamic and fully-dynamic solvers (e.g., Thomas et al., 2014; Erickson et al.,
273 2023). Also, the location where the second rupture nucleates after jumping across the step-over is
274 different (blue star in Figure c,e,g). It is shallower in our simulation. This test shows that the
275 rupture speed and nucleation behavior are indeed sensitive to the solution method and whether
276 stress transfer is dynamic or quasistatic. Nevertheless, the distribution of slip is similar in all
277 three simulations, showing that the final magnitude and stress drop distributions calculated with
278 Quake-DFN are valid.

279

280 3.3 Comparison Study 3- fault branching

281 The last comparison study considers a branching fault system. We compare our modeling
282 with the solution obtained with FaultMod to the TPV18 benchmark test of the SCEC/USGS
283 Spontaneous Rupture Code Verification Project (Harris et al., 2009, 2018). The TPV18 exercise
284 solves a single earthquake rupture with a 30-degree branch fault (Harris et al., 2018). Again,
285 since the FaultMod is a fully dynamic solver with slip-weakening friction, it would not give a
286 solution identical to our quasi-dynamic rate and state friction solution. However, the two
287 solutions should be comparable when the parameters lead to a similar magnitude of friction drop.
288 Following the TPV18 problem description, the initial stress tensor is depth-dependent, and the
289 initial stress on the branch fault is lower than that on the main fault at the same depth (figure 4a).
290 We set $a=0.006$, $b=0.013$, $D_c=1\text{mm}$, $\theta_i = 10^{10}$, and $V_i = 10^{-12}$ to achieve dynamic friction ~ 0.12 .
291 This setup produces a similar magnitude of stress drop to the benchmark simulation (Figure 4)

292 Our simulation result is again comparable to the FaultMod solution for the benchmark
293 simulation. The evolution of stress and slip predicted by FaultMod at a selection of points is
294 provided on the website of the SCEC/USGS Spontaneous Rupture Code Verification Project
295 (figure 5b). We calculated the displacement and stress evolution at those points and found them
296 very similar to those obtained with FaultMod (figure 5). The fault slip decreases near the surface
297 (figure 5a) because the stress drop is insignificant there due to the low initial stress. One
298 significant difference is that the shallow rupture initiates earlier in our simulation (blue solid
299 lines) than in the FaultMod solution (blue dashed line). This is presumably due to the quasistatic
300 stress transfer, which immediately changes stresses everywhere.

301

302 **4. Injection Induced Earthquakes on a Planar Fault**

303 In this set of simulations, we investigate the effect of an injection into a planar fault. This
 304 problem has also been treated in several previous studies (Larochelle et al., 2021; Galis et al.,
 305 2017; Garagash and Germanovich, 2012; Saez and Lecampion, 2023). They showed that,
 306 depending on the initial stress, rupture might either be ‘self-arrested’, meaning that it is confined
 307 to the area of increased pore pressure, or might run away outside of it. The runaway rupture can
 308 occur when the dynamic friction (μ_d , the friction at the end of the rupture) is smaller than initial
 309 friction μ_i , i.e., $\mu_i - \mu_d > 0$ (Garagash and Germanovich, 2012). The dynamic friction μ_d can be
 310 approximated in rate and state formulation as steady-state residual friction at the rupture peak
 311 slip rate (V_p): $\mu_f = \mu_0 + (a-b)\log(V_p/V_0)$ (Larochelle et al., 2021). One may approximate the rupture
 312 peak slip speed $V_p = 1\text{m/s}$, and then the runway potential can be defined as

313
$$\mu_i - \mu_f = \mu_i - \mu_0 + (a - b) \log(V_0) \quad (7)$$

314 or equivalently from equation 2,

315
$$\mu_i - \mu_f = a \log(V_i) + b \log\left(\frac{\theta_i}{D_c}\right). \quad (8)$$

316 The approximated condition for runaway rupture is $\mu_i - \mu_f > 0$. Equations 7 and 8 imply that, in
 317 terms of the model parameters and initial conditions, the rupture magnitude should be primarily
 318 dependent on $\mu_i - \mu_0$ (equation 7), hence on the initial values of V_i and θ_i (equation 8).

319 We consider a $10 \times 7\text{ km}$ vertical planar fault with an $8 \times 5\text{ km}$ unstable fault patch
 320 (figure 1a). Unstable fault has $a = 0.003$ and $b = 0.006$. The fault area around that patch is rate-
 321 strengthening with $a = 0.006$ and $b = 0.003$. D_c is set to $200\mu\text{m}$ everywhere. Normal stress
 322 gradient is 7 kpa/m (figure 1d). The element size is 50 m for the unstable zone and 100m for the

323 stable zone. A lumped mass $M = 10^6 \text{kg/m}^2$ is assigned to each element. The injector is located at
324 2.5km depth with a flow rate of $0.1 \text{m}^3/\text{s}$ (100kg/s) and a permeability of 10^{-16}m^2 . We conducted
325 three simulations with constant $\mu_0 = 0.3$ and different initial conditions going from less to more
326 critical: (i) $V_i = 10^{-30}$ and $\theta_i = 10^6$, (ii) $V_i = 10^{-20}$ and $\theta_i = 10^3$, and (iii) $V_i = 10^{-15}$ and $\theta_i = 10^9$.
327 According to equation 8, $\mu_i - \mu_f$ of each case is (i) -0.073, (ii) -0.046, and (iii) 0.072, implying
328 that only the third case has a high potential for runaway rupture since $\mu_i - \mu_f > 0$.

329 As found in previous studies, our simulations show self-arrested and run-away ruptures.
330 The self-arrested rupture occurs when $\mu_i - \mu_f < 0$ (low V_i and θ_i ; figure 6a-h). In this regime, the
331 magnitudes of the induced earthquake increase with time (and with injection volume since the
332 injection rate is constant). The earthquake is smaller in the early stage (figure 6a,e) and grows
333 larger in the later stage (figure 6b,f). Conversely, when $\mu_i - \mu_f > 0$ (high V_i and θ_i ; figure 6i-l),
334 run-away rupture occurs at the very early stage (figure 6i). The fault run-away potential resets
335 after the initial run-away rupture, and self-arrested rupture occurs within the unstable zone
336 (figure 6j).

337 In the self-arrested rupture sequences, the induced earthquakes nucleate near the injector
338 and migrate away with time (figure 6d,h). Most of the large events are nucleated slightly away
339 ($>500\text{m}$) but not too far ($<2000\text{m}$) from the injector. This is likely due to the fact that the high
340 pressure near the injector stabilizes fault slip in the rate and state framework (according to
341 equation 5) as observed in previous simulations and in-situ experiments (Guglielmi et al., 2015;
342 Bhattacharya and Viesca, 2019; Cappa et al., 2019; Larochelle et al., 2021). These simulations
343 show the potential of our simulator to gain insight into the factors controlling the timing and
344 magnitudes of sequences of induced earthquakes in the particular simple case of a single planar
345 fault.

346

347 **5. Injection Induced Earthquakes on a Branching Fault Systems**

348 We now move to a more complex setup where fluid is injected into a secondary fault that
349 is branching out from a larger fault (Figures 1b and 7). Both faults are assumed planar. This set
350 of simulations was designed to show that our simulator can be used to explore how the branching
351 fault geometry relative to the regional stress field affects induced seismicity. We consider two
352 strike-slip faults at two different angles (90° and 60° in Figures 7a and b). Both faults are
353 unstable ($a = 0.003$, $b = 0.006$, and $D_c = 200\mu\text{m}$) but with a shallow stable zone at a depth less
354 than 500m ($a = 0.006$, $b = 0.003$, and $D_c = 200\mu\text{m}$) (figure 1b). Lumped mass $M = 10^7\text{kg/m}^2$ is
355 assigned to each element. One fault is longer ($4\text{km} \times 3\text{km}$) than the other fault ($2\text{km} \times 3\text{km}$). The
356 element size is uniform and equal to $70 \times 70\text{m}$. The injector is located at 1.5km depth at the
357 center of the shorter fault with a flow rate of $0.03 \text{ m}^3/\text{s}$ (30kg/s). We assume a permeability of
358 $3 \times 10^{-16} \text{ m}^2$ for all simulations. The simulations run for 50k timesteps, sufficiently covering a
359 time duration of 1 year.

360 We conducted simulations by varying the maximum stress orientation by increments of
361 15° (Figure 7a and b dashed lines). Maximum stress has a depth gradient of 10kPa/m , and
362 minimum stress is assumed to be 50% of maximum. The initial stress and friction are determined
363 based on the stress orientation and magnitude. The value of $\mu_i - \mu_f$, which defines the run-away
364 potential, is determined by the maximum stress angle (that determines μ_i) and μ_0 (that determines
365 μ_f , equation 7). To test the influence of $\mu_i - \mu_f$, we vary μ_0 between $0.32 \sim 0.48$. We assume a
366 uniform initial state variable $\theta_i = 10^8\text{s}$ (3 years), and initial velocity V_i is determined based on
367 equation (2). Since θ_i is constant, the potential for a run-away rupture is determined by V_i . If the

368 faults are optimally oriented to the stress field, V_i is high (figure 7c). Conversely, if faults are
369 non-optimally oriented, V_i is low (figure 7d).

370 The two-fault simulations illustrate the effects of the initial stress field and faults
371 interaction. We find the rupture occurs in the one-year time window of the simulation if the fault
372 is near optimally oriented (30° and 45° from maximum stress orientation; figure 8). The main
373 fault (blue) ruptures only when the maximum stress angle is ± 45 or ± 30 , and the branch fault
374 (red) only ruptures when the maximum strike angle is $\pm 60^\circ$ or $\pm 45^\circ$ in panel a and -30° , -15° , and
375 75° in panel b. The main fault rupture is well predicted by run-away potential as it only ruptures
376 when $\mu_i - \mu_f > 0$. The magnitude of the maximum event increases as μ_0 decreases (*i.e.*, run-away
377 potential increases). The results, together with the planar fault simulation results presented in
378 section 4, show that the risk of an induced earthquake can be primarily determined by run-away
379 potential ($\mu_i - \mu_f$).

380 In all cases, the main fault (blue) ruptures only when μ_0 is low enough, while the branch
381 fault (red) ruptures up to a much higher μ_0 value as long as the fault is near-optimally oriented.
382 This is expected since the branch fault is submitted to larger poro-elastic stresses than the main
383 fault which is farther away from the injection. The main fault is loaded mainly by slip on the
384 branch fault, whether seismic or aseismic (*i.e.*, faults interaction).

385 The interactions comply with the prescribed stress field. For instance, in the case of a
386 maximum stress orientation of 45° , the slip on the branch fault is left-lateral (figure 9a). It
387 reduces normal stress on the north side of the main fault, causing the earthquake in the main fault
388 to propagate toward the north first. The reverse happens in the case of a maximum stress
389 orientation of -45° , where the branch fault is right-lateral, and the main fault earthquake
390 propagates toward the south first (figure 9b). In the 60° angle fault geometry with maximum

391 stress orientation -30° , the triggered rupture propagates both north and south (figure 9d). This is
392 due to the normal stress effect competing with the shear stress effect. In the northern part of the
393 blue fault, both normal and shear stress are increased, and the opposite occurs in the southern
394 part. Also, we find that an aseismic-to-seismic interaction can occur, as observed in the Brawley
395 geothermal field, where injection-induced aseismic slip on a shallow normal fault triggered a
396 strike-slip earthquake on a deeper fault (Im and Avouac, 2021b). Aseismic slip on the non-
397 optimally oriented fault can trigger earthquakes in the other optimally oriented fault (figure 9c).

398

399 **6. A realistic case example – The Prague earthquake sequence, Oklahoma**

400 The simulation is designed to approximate the geometry of the Wilzetta fault system,
401 which ruptured during the Prague (Oklahoma) earthquake sequence in 2011 (Karanen et al.,
402 2013; Sumy et al., 2014). The sequence consists of a cascade of three larger events of magnitude
403 M 5.0, 5.7, and 5.0, which occurred within 3 days. The injection began in 1993, and the flow rate
404 was kept under $1500\text{m}^3/\text{month}$ ($\sim 0.58\text{kg/s}$; Karanen et al., 2013). No earthquake had been
405 reported on that fault system until a M4.1 event in February 2010. The Prague earthquake
406 sequence occurred in November 2011.

407 The geometry and injection location (figure 10) are adopted from Karanen et al. (2013)
408 with the addition of the faults ruptured by the 5.7 and 5.0, which had not been recognized prior
409 to the earthquake sequence. The faults were discretized with an element size of 200m. The
410 simulation assumes a maximum stress (σ_I) orientation $\sim N80^\circ E$ (Sumy et al., 2013). The point
411 source injector is located at a depth of 1500m. We used a constant flow rate of 0.27kg/s (~ 700

412 m^3/month), which is a rough average of the actual flow rate between 1993-2011 (Keranen et al.,
413 2013), with a permeability of $3 \times 10^{-18} \text{m}^2$.

414 For the sensitivity test, a total of 36 simulations were conducted: we tested two values of
415 θ_i (300 years, 30k years), three values of σ_1 orientations (75° , 80° , 85° N; figure 10b), and six
416 values of μ_0 for each of the stress setups. The minimum stress is set as half of the maximum
417 stress, $\sigma_3/\sigma_1 = 0.5$, since we found by trial and error that this ratio best reproduces the observed
418 earthquake sequence. The range of μ_0 is determined to cover the mainshock ruptured/unruptured
419 scenarios ($\mu_0 = 0.28 \sim 0.33$). The maximum horizontal stress gradient is 10kpa/m.

420 Because the initial stress and friction parameters are prescribed, the run-away potential of
421 each fault (equation 7) is determined only by its orientation (i.e., μ_i) and the value of μ_f ($= \mu_0 + (a -$
422 $b)\log(V_p/V_0)$). In general, we find that the mainshock tends to occur earlier and reach a larger
423 magnitude at lower μ_0 (equivalently, μ_f) and a smaller stress angle (figure 11). Most of the $M > 5$
424 mainshocks occur within 10 years except the high θ case with a stress angle of 77.5° (figure
425 11d). The maximum magnitude is typically larger than 5 if the initial run-away potential is large
426 (i.e., μ_0 is small). The maximum magnitude is abruptly reduced at a particular point of μ_0 . For
427 example, in the case $\theta_i = 10^\circ$ s and maximum stress orientation 80° , this happens between $\mu_0 =$
428 0.31 and 0.32 (figure 11b). This is because the mainshock fault rupture was not triggered. In all
429 cases, earthquakes nucleate near the injector and propagate southwestward (figure 12). This
430 process corresponds to the actual sequence of the 2012 Prague earthquake. If the μ_0 is low,
431 rupture propagates all the way down to the SW mainshock fault (figure 12a and b). If the μ_0 is
432 high, the initial rupture is arrested before it reaches the SW mainshock fault (figure 12c), making
433 the earthquake magnitude significantly lower. This is why the maximum magnitude is
434 significantly smaller in the mainshock non-triggered cases (i.e., x-marked cases in figure 11a and

435 b). If the potential for run-away rupture is very high, the rupture also propagates toward the NE
436 fault (figure 12a), which did not happen in the actual Prague sequence.

437 In the actual Prague earthquake sequence, the mainshock occurred \sim 1 day after the M5.0
438 foreshock. We find this time lag can result if the foreshock rupture is arrested before but close to
439 the mainshock fault (i.e., somewhere between figure 12b and 12c). In this case, the mainshock is
440 triggered after a delay due to its own nucleation time. One of our simulation sets could reproduce
441 this delayed triggering. When the initial rupture is arrested near the mainshock fault (figure 13b),
442 the mainshock fault ruptures after a day of nucleation period (figure 13c). To check if this occurs
443 in the other simulation set, we conducted extra simulations in between the figure 12b and c cases.
444 We found $\mu_0 = 0.3155$ results in the \sim 1-day delay between foreshock and aftershock (figure 13d-
445 f). Interestingly, those delayed mainshocks propagate back into the foreshock fault, making the
446 fault re-ruptured (figure 13c and f).

447 Our simulations could not reproduce the M5 aftershock (figure 10b; green fault). The
448 reason is twofold: (i) the initial potential for run-away rupture on the fault that produced this
449 aftershock is too low due to its non-optimal orientation, and (ii) the Coulomb stress on the
450 aftershock fault decreases during the foreshock and mainshock sequence. This is in line with the
451 Coulomb stress analysis conducted in a previous study (Sumy et al., 2013). It is evident that this
452 particular aftershock cannot be solely attributed to fault interaction in a system of faults with the
453 same friction properties and submitted to the same stress tensor. Some other factor is needed to
454 explain the occurrence of this event (e.g., local stress heterogeneities or a lower dynamic friction
455 μ_f , on that particular fault).

456

457 **7. Discussion**

458 The comparison studies presented above are satisfying, and the application examples
459 demonstrate that Quake-DFN can be used to simulate real-case examples of induced seismicity
460 due to its computational efficiency. All the simulations presented in this study were calculated on
461 a standard desktop computer (CPU: i9-13900k), and calculation times for each simulation range
462 <10 minutes (branch fault simulation in section 5; 3741 elements), 15-20 minutes (Prague
463 earthquake in section 6; 6220 elements) and 1.5-2 hours (planar fault simulations in section 4;
464 20200 elements). The simulation speed with a large element size can be further improved by
465 utilizing H-matrix approximation (Borm et al., 2003) in the future.

466 In the simulations presented in sections 4-6, the normal stress is depth-dependent (figures
467 2d-f). In this case, the critical stiffness for each element is also depth-dependent, so the critical
468 length decreases with depth, allowing localized smaller earthquakes in deeper areas. As a result,
469 the deeper part of our fault models may contain under-resolved inherently discrete elements,
470 where fault ruptures can occur at a single element. For instance, for the planar fault case ($D_c =$
471 $200\mu\text{m}$ and normal stress gradient 7kPa/m), assuming $\gamma = 1$, L_c (equation 5) becomes smaller
472 than our minimum element length (50m) at a depth $> 3.8\text{km}$. This is deeper than the injection
473 depth of 2.5km. The simulation is well resolved near the injector, but in the deeper area, single-
474 element ruptures are allowed. This is the major source of the small aftershocks in our simulation
475 (small earthquakes in figures 6 and 11). We kept the deeper area under-resolved here to limit
476 computational time. However, users can choose to avoid this issue by adjusting grid size, normal
477 stress, or friction parameters in deep areas since Quake-DFN does not have restrictions on the
478 element size.

479 The simulations presented in this study are restricted to strike-slip motion. The code also
480 allows dip-slip motion. It can be expanded in the future to allow for a mixed mode by using two
481 shear stiffness matrices. In this case, the rake direction should be calculated in each timestep
482 according to the maximum stress orientation.

483 The simulation of induced earthquakes does not require including tectonic loading
484 (Dieterich et al., 2015), which is not necessary to simulate a sequence driven by tectonic stresses
485 over a short period of time (short with respect to the return period of the largest event in the
486 region of interest) (Im and Avouac, 2023). However, to simulate earthquake sequences driven by
487 tectonics over a longer period of time, tectonic loading would need to be included. Using the
488 current implementation of Quake-DFN, the long-term loading of a network of non-planar faults
489 would result in a rapid build-up of elastic stresses at the fault tips and fault kinks. In nature,
490 stress build-up would be limited by the yielding of the bulk material surrounding the faults. A
491 backslip approach could be adopted to address this issue in a cost-effective way, as done in
492 RSQSim (Richards-Dinger and Dietrich et al., 2012) or MCQSim (Zielke and Mai, 2023).
493 Another approach would be to take off-fault deformation into account (e.g., Okubo et al., 2020),
494 but that would come at an additional computational cost. Simulation of tectonically loaded faults
495 should also, in principle, take into account postseismic processes. Quake-DFN naturally
496 produces afterslips on rate-strengthening or conditionally stable faults but would not account for
497 viscoelastic postseismic relaxation. Viscoelastic relaxation is generally observed after $M > 7$
498 events and can significantly impact the spatio-temporal distribution of seismicity (e.g., Pollitz et
499 al., 2002). ViscoSim (Pollitz, 2012) was developed specifically to address that issue. It might be
500 possible to include the effect of visco-elastic relaxation in Quake-DFN by modulating tectonic
501 loading following the approach adopted in MCQSim.

502 In the simulations presented in this study, we used an analytical solution to represent the
503 poroelastic stress change from the injection. Although this approximation could produce a
504 realistic earthquake sequence, correctly defining pressure diffusion is another important
505 ingredient for injection-induced earthquake forecast. A more realistic model could actually be
506 used since our simulator is ready for coupling stress change calculated from external
507 geomechanical models, for example, Tough-FLAC coupled simulator (e.g., Rutqvist et al., 2002;
508 Taron et al., 2009; Im et al., 2021c) as an input parameter of τ^E and σ^E in equation 1. This is a
509 one-way coupling, but eventually, fully coupled earthquake simulation would be necessary to
510 accommodate the permeability change that can result from fault reactivation (e.g., Guglielmi et
511 al., 2015; Im et al., 2018).

512 Our simulation (sections 4 and 5) shows that larger induced earthquakes occur earlier if
513 the run-away potential, $\mu_i - \mu_f$ (equation 7 or 8), is high. This quantity captures the effect of the
514 initial stress on induced ruptures observed in numerical studies (Garagash and Germanovich,
515 2012; Dieterich et al., 2015; Larochelle et al., 2021). This quantity also determines the variation
516 of co-seismic slip measured along a fault with varying orientations (Milliner et al., 2022). Each
517 parameter entering this quantity can be estimated based on the local stress field and fault
518 orientation (μ_i) or derived from laboratory friction measurements ($\mu_f = \mu_0 - (a-b)\log(V_0)$). Given
519 the importance on the rupture timing and magnitude, our simulation confirms this value should
520 be primarily considered to assess the risk of injection-induced earthquakes.

521 Some of the parameters entering our simulations are, in principle, measurable or inferred
522 from laboratory studies. However, due to the uncertainty of the measurement and the
523 heterogeneity in actual fault systems (e.g., Cattania and Segall 2021), it may be more practical to
524 explore a wide range of parameter space to select possible sets of parameters and initial

525 conditions. Such an approach for seismic hazard assessment would be possible with the
526 simulator presented in his study, given its low computational cost.

527 **8. Conclusion**

528 This study presents an earthquake simulator consistent with more advanced simulations
529 of seismic ruptures while allowing for numerically efficient simulations of induced earthquake
530 sequences. We, therefore, believe that the tool will be useful to gain insight into the factors
531 controlling the time and magnitude of induced earthquakes. Some limitations of the current
532 version of Quake-DFN can be addressed in future work, for example, by allowing for a variable
533 rake angle or by facilitating the representation of non-planar fault using a triangular mesh.
534 Further improvements would be needed to allow simulations of earthquake sequences driven by
535 tectonic loading only.

536

537 **Data and Resources**

538 All simulation results in this article are generated by Quake-DFN. The simulator and source code
539 are provided on GitHub (<https://github.com/limkjae/Quake-DFN>) and the GMG center web page
540 (<https://gmg.caltech.edu>). The supplementary material includes one figure (Figure S1) and one
541 text (Text S1), discussing the influence of α value in equation 3. Simulation results with varied α
542 values are shown in Figure S1 and discussed in Text S1.

543

544 **Declaration of Competing Interests**

545 The authors acknowledge that there are no conflicts of interest recorded.

546

547 **Acknowledgment**

548 We thank associate editor Arben Pitarka and an anonymous reviewer for their insightful and
549 constructive evaluations. This study was supported by the National Science Foundation (award
550 #1822214) via the IUCR center Geomechanics and Mitigation of Geohazards.

551

552

553 **References**

554 Acosta, M., J. Avouac, J. D. Smith, K. Sirorattanakul, H. Kaveh, and S. J. Bourne (2023).
555 Earthquake nucleation characteristics revealed by seismicity response to seasonal stress
556 variations induced by gas production at Groningen, *Geophys. Res. Lett.* 50, e2023GL105455,
557 doi: 10.1029/2023GL105455.

558 Alghannam, M., and R. Juanes (2020). Understanding rate effects in injection-induced
559 earthquakes, *Nat. Commun.* 11, no. 1, 3053.

560 Barbot, S. (2019). Slow-slip, slow earthquakes, period-two cycles, full and partial ruptures, and
561 deterministic chaos in a single asperity fault, *Tectonophysics* 768, 228171.

562 Ben-Zion, Y. (1996). Stress, slip, and earthquakes in models of complex single-fault systems
563 incorporating brittle and creep deformations, *J. Geophys. Res.* 101, 5677–5706.

564 Bhattacharya, P., and R. C. Viesca (2019). Fluid-induced aseismic fault slip outpaces pore-fluid
565 migration, *Science* 364, 464–468.

566 Borm, S., L. Grasedyck, and W. Hackbusch (2003). Introduction to hierarchical matrices with
567 applications, *Eng. Anal. Bound. Elem.* 5, 405–422.

568 Bourne, S. J., and S. J. Oates (2017). Extreme threshold failures within a heterogeneous elastic
569 thin sheet and the spatial-temporal development of induced seismicity within the Groningen gas
570 field, *J. Geophys. Res.* 122, 10–299.

571 Candela, T., C. G. Machado, O. Leeuwenburgh, and J. T. Heege (2022). A physics-informed
572 optimization workflow to manage injection while constraining induced seismicity: The
573 Oklahoma case, *Front. Earth Sci.* 10, 1053951.

574 Candela, T., B. Wassing, J. T. Heege, and L. Buijze (2018). How earthquakes are induced.
575 *Science* 360, 598–600.

576 Cappa, F., Y. Guglielmi, and L. D. Barros (2022). Transient evolution of permeability and
577 friction in a slowly slipping fault activated by fluid pressurization, *Nat. Commun.* 13, 3039.

578 Cappa, F., M. M. Scuderi, C. Collettini, Y. Guglielmi, and J.-P. Avouac (2019). Stabilization of
579 fault slip by fluid injection in the laboratory and in situ, *Sci. Adv.* 5, doi:
580 10.1126/sciadv.aau4065.

581 Cattania, C., and P. Segall (2021). Precursory slow slip and foreshocks on rough faults, *J.*
582 *Geophys. Res.* 126, e2020JB020430, doi: 10.1029/2020JB020430.

583 Dieterich, J. H. (1979). Modeling of rock friction: 1. Experimental results and constitutive
584 equations, *J. Geophys. Res.* 84, 2161–2168.

585 Dieterich, J. H., K. B. Richards-Dinger, and K. A. Kroll (2015). Modeling injection-induced
586 seismicity with the physics-based earthquake simulator RSQSim, *Seismol. Res. Lett.* 86, 1102–
587 1109.

588 Ellsworth, W. L. (2013). Injection-induced earthquakes, *Science* 341, doi:
589 10.1126/science.1225942.

590 Erickson, B. A., J. Jiang, M. Barall, N. Lapusta, E. M. Dunham, R. Harris, L. S. Abrahams, K. L.
591 Allison, J. P. Ampuero, S. Barbot, et al. (2020). The community code verification exercise for
592 simulating sequences of earthquakes and aseismic slip (SEAS), *Seismol. Res. Lett.* 91, 874–890.

593 Erickson, B. A., J. Jiang, V. Lambert, S. D. Barbot, M. Abdelmeguid, M. Almquist, J. P.
594 Ampuero, R. Ando, C. Cattania, A. Chen, et al. (2023). Incorporating full elastodynamic effects
595 and dipping fault geometries in community code verification exercises for simulations of
596 earthquake sequences and aseismic slip (SEAS), *Bull. Seismol. Soc. Am.* 113, 499–523.

597 Galis, M., J. P. Ampuero, P. M. Mai, and F. Cappa (2017). Induced seismicity provides insight
598 into why earthquake ruptures stop, *Sci. Adv.* 3, doi: 10.1126/sciadv.aap7528.

599 Garagash, D. I., and L. N. Germanovich (2012). Nucleation and arrest of dynamic slip on a
600 pressurized fault, *J. Geophys. Res.* 117, doi: 10.1029/2012JB009209.

601 Goebel, T. H. W., and E. E. Brodsky (2018). The spatial footprint of injection wells in a global
602 compilation of induced earthquake sequences, *Science* 361, 899–904, doi:
603 10.1126/science.aat5449.

604 Guglielmi, Y., F. Cappa, J.-P. Avouac, P. Henry, and D. Elsworth (2015). Seismicity triggered
605 by fluid injection-induced aseismic slip, *Science* 348, 1224–1226, doi: 10.1126/science.aab0476.

606 Hager, B. H., J. Dieterich, C. Frohlich, R. Juanes, S. Mantica, J. H. Shaw, F. Bottazzi, F.
607 Caresani, D. Castineira, A. Cominelli, et al. (2021). A process-based approach to understanding
608 and managing triggered seismicity, *Nature* 595, 684–689.

609 Harris, R. A., M. Barall, B. Aagaard, S. Ma, D. Roten, K. Olsen, B. Duan, D. Liu, B. Luo, K.
610 Bai, et al. (2018). A suite of exercises for verifying dynamic earthquake rupture codes, *Seismol.*
611 *Res. Lett.* 89, 1146–1162.

612 Harris, R. A., M. Barall, R. Archuleta, E. Dunham, B. Aagaard, J. P. Ampuero, H. Bhat, V.
613 Cruz-Atienza, L. Dalguer, P. Dawson, et al. (2009). The SCEC/USGS dynamic earthquake
614 rupture code verification exercise, *Seismol. Res. Lett.* 80, 119–126.

615 Im, K., and J.-P. Avouac (2021a). On the role of thermal stress and fluid pressure in triggering
616 seismic and aseismic faulting at the Brawley Geothermal Field, California, *Geothermics* 97,
617 102238, doi: 10.1016/j.geothermics.2021.102238.

618 Im, K., and J.-P. Avouac (2021b). Tectonic tremor as friction-induced inertial vibration, *Earth*
619 *Planet. Sci. Lett.* 576, 117238, doi: 10.1016/j.epsl.2021.117238.

620 Im, K., and J.-P. Avouac (2023). Cascading foreshocks, aftershocks and earthquake swarms in a
621 discrete fault network, *Geophys. J. Int.* 235, 831–852.

622 Im, K., J.-P. Avouac, E. R. eimisson, and D. Elsworth (2021). Ridgecrest aftershocks at Coso
623 suppressed by thermal destressing, *Nature* 595, 70–74.

624 Im, K., D. Elsworth, and Y. Fang (2018). The influence of Preslip sealing on the permeability
625 evolution of fractures and faults, *Geophys. Res. Lett.* 45, doi: 10.1002/2017GL076216.

626 Im, K., D. Elsworth, C. Marone, and J. Leeman (2017). The impact of frictional healing on stick-
627 slip recurrence interval and stress drop: Implications for earthquake scaling, *J. Geophys. Res.*
628 doi: 10.1002/2017JB014476.

629 Jiang, J., B. A. Erickson, V. R. Lambert, J. P. Ampuero, R. Ando, S. D. Barbot, C. Cattania, L.
630 D. Zilio, B. Duan, E.M. Dunham, et al. (2022). Community-driven code comparisons for three-
631 dimensional dynamic modeling of sequences of earthquakes and aseismic slip, *J. Geophys. Res.*
632 127, e2021JB023519, doi: 10.1029/2021JB023519.

633 Keranen, K. M., H. M. Savage, G. A. Abers, and E. S. Cochran (2013). Potentially induced
634 earthquakes in Oklahoma, USA: Links between wastewater injection and the 2011 Mw 5.7
635 earthquake sequence, *Geology* 41, 699–702.

636 Kroll, K. A., J. H. Dieterich, K. B. Richards-Dinger, and D. D. Oglesby (2023). 3-D Simulations
637 of earthquakes rupture jumps: 1. Homogeneous pre-stress conditions, *Geophys. J. Int.* 234, 395–
638 403.

639 Langenbruch, C., and M. D. Zoback (2016). How will induced seismicity in Oklahoma respond
640 to decreased saltwater injection rates? *Sci. Adv.* 2, e1601542, doi: 10.1126/sciadv.1601542.

641 Lapusta, N., J. R. Rice, Y. Ben-Zion, and G. Zheng (2000). Elastodynamic analysis for slow
642 tectonic loading with spontaneous rupture episodes on faults with rate-and state-dependent
643 friction, *J. Geophys. Res.* 105, 23,765–23,789.

644 Laroche, S., N. Lapusta, J. Ampuero, and F. Cappa (2021). Constraining fault friction and
645 stability with fluid-injection field experiments, *Geophys. Res. Lett.* 48, e2020GL091188, doi:
646 10.1029/2020gl091188.

647 Lee, K. K., W. L. Ellsworth, D. Giardini, J. Townend, S. Ge, T. Shimamoto, I. W. Yeo, T. S.
648 Kang, J. Rhee, D.H. Sheen, et al. (2019). Managing injection-induced seismic risks, *Science* 364,
649 730–732.

650 Linker, M. F., and J. H. Dieterich (1992). Effects of variable normal stress on rock friction:
651 Observations and constitutive equations, *J. Geophys. Res.* 97, no. B4, 4923, doi:
652 10.1029/92JB00017.

653 Madariaga, R. (1976). Dynamics of an expanding circular fault, *Bull. Seismol. Soc. Am.* 66,
654 639–666.

655 Marone, C. (1998). Laboratory-derived friction laws and their application to seismic faulting,
656 *Annu. Rev. Earth Planet. Sci.* 26, 643–696, doi: 10.1146/annurev.earth.26.1.643.

657 McGarr, A. (2014). Maximum magnitude earthquakes induced by fluid injection, *J. Geophys.*
658 *Res.* 119, 1008–1019.

659 Milliner, C. W. D., S. Aati, and J.-P. Avouac (2022). Fault friction derived from fault bend
660 influence on coseismic slip during the 2019 Ridgecrest Mw 7.1 mainshock, *J. Geophys. Res.*
661 127, e2022JB024519, doi: 10.1029/2022JB024519.

662 Norbeck, J. H., and J. L. Rubinstein (2018). Hydromechanical earthquake nucleation model
663 forecasts onset, peak, and falling rates of induced seismicity in Oklahoma and Kansas, *Geophys.*
664 *Res. Lett.* 45, 2963–2975.

665 Okada, Y. (1992). Internal deformation due to shear and tensile faults in a half-space, *Bull.*
666 *Seismol. Soc. Am.* 82, 1018–1040.

667 Okubo, K., E. Rougier, Z. Lei, and H. S. Bhat (2020). Modeling earthquakes with off-fault
668 damage using the combined finite-discrete element method, *Comput. Part. Mech.* 7, 1057–1072.

669 Olsen, K. B., R. Madariaga, and R. J. Archuleta (1997). Three-dimensional dynamic simulation
670 of the 1992 Landers earthquake, *Science* 278, 834–838.

671 Pollitz, F. F. (2012). ViscoSim earthquake simulator, *Seismol. Res. Lett.* 83, 979–982

672 Pollitz, F. F., and I. S. Sacks (2002). Stress triggering of the 1999 Hector Mine earthquake by
673 transient deformation following the 1992 Landers earthquake, *Bull. Seismol. Soc. Am.* 92, 1487–
674 1496.

675 Rice, J. R. (1993). Spatio-temporal complexity of slip on a fault, *J. Geophys. Res.* 98, 9885, doi:
676 10.1029/93JB00191.

677 Richards-Dinger, K., and J. H. Dieterich (2012). RSQSim earthquake simulator, *Seismol. Res.*
678 *Lett.* 83, no. 6, 983–990.

679 Rudnicki, J. W. (1986). Fluid mass sources and point forces in linear elastic diffusive solids,
680 *Mech. Mater.* 5, 383–393.

681 Rutqvist, J., Y.-S. Wu, C.-F. Tsang, and G. Bodvarsson (2002). A modeling approach for
682 analysis of coupled multiphase fluid flow, heat transfer, and deformation in fractured porous
683 rock, *Int. J. Rock Mech. Min. Sci.* 39, 429–442, doi: 10.1016/S1365-1609(02)00022-9.

684 Sáez, A., and B. Lecampion (2024). Fluid-driven slow slip and earthquake nucleation on a slip-
685 weakening circular fault, *J. Mech. Phys. Solids* 183, 105506, doi: 10.1016/j.jmps.2023.105506.

686 Segall, P., and S. Lu (2015). Injection-induced seismicity: Poroelastic and earthquake nucleation
687 effects, *J. Geophys. Res.* 120, 5082–5103.

688 Shaw, B. E., K. R. Milner, E. H. Field, K. Richards-Dinger, J. J. Gilchrist, J. H. Dieterich, and T.
689 H. Jordan (2018). A physics-based earthquake simulator replicates seismic hazard statistics
690 across California, *Sci. Adv.* 4, eaau0688, doi: 10.1126/sciadv.aau0688.

691 Sumy, D. F., E. S. Cochran, K. M. Keranen, M. Wei, and G. A. Abers (2014). Observations of
692 static Coulomb stress triggering of the November 2011 M5.7 Oklahoma earthquake sequence, *J.*
693 *Geophys. Res.* 119, 1904–1923, doi: 10.1002/2013JB010612.

694 Taron, J., D. Elsworth, and K.-B. Min (2009). Numerical simulationof thermal-hydrologic-
695 mechanical-chemical processes in deformable,fractured porous media, Int. J. Rock Mech. Min.
696 Sci. 46, 842–854, doi: 10.1016/j.ijrmms.2009.01.008.

697 Thomas, M. Y., N. Lapusta, H. Noda, and J. Avouac (2014). Quasidynamic versus fully dynamic
698 simulations of earthquakes and aseismic slip with and without enhanced coseismic weakening, J.
699 Geophys. Res. 119, 1986–2004.

700 Viesca, R. C., and D. I. Garagash (2018). Numerical methods for coupled fracture problems, J.
701 Mech. Phys. Solids 113, 13–34.

702 Wang, T. A., and E. M. Dunham (2022). Hindcasting injectioninduced aseismic slip and
703 microseismicity at the Cooper Basin

704 Enhanced Geothermal Systems Project, Sci. Rep. 12, 19481.

705 Zhai, G., M. Shirzaei, and M. Manga (2020). Elevated seismic hazard in Kansas due to high-
706 volume injections in Oklahoma, Geophys. Res. Lett. 47, e2019GL085705, doi:
707 10.1029/2019GL085705.

708 Zielke, O., and P. M. Mai (2023). MCQsim: A multicycle earthquake simulator, Bull. Seismol.
709 Soc. Am. 113, 889–908.

710 Zoback, M. D., and S. M. Gorelick (2012). Earthquake triggering and large-scale geologic
711 storage of carbon dioxide, Proc. Natl. Acad. Sci. 109, no. 26, 10164–10168.

712 **Author Affiliations**

713 **Kyungjae Im** (Corresponding author: kjim@caltech.edu)

714 Geology and Planetary Science Division, California Institute of Technology, Pasadena, CA

715 91125, United States

716

717 **Jean-Philippe Avouac**

718 Geology and Planetary Science Division, California Institute of Technology, Pasadena, CA

719 91125, United States

720 *

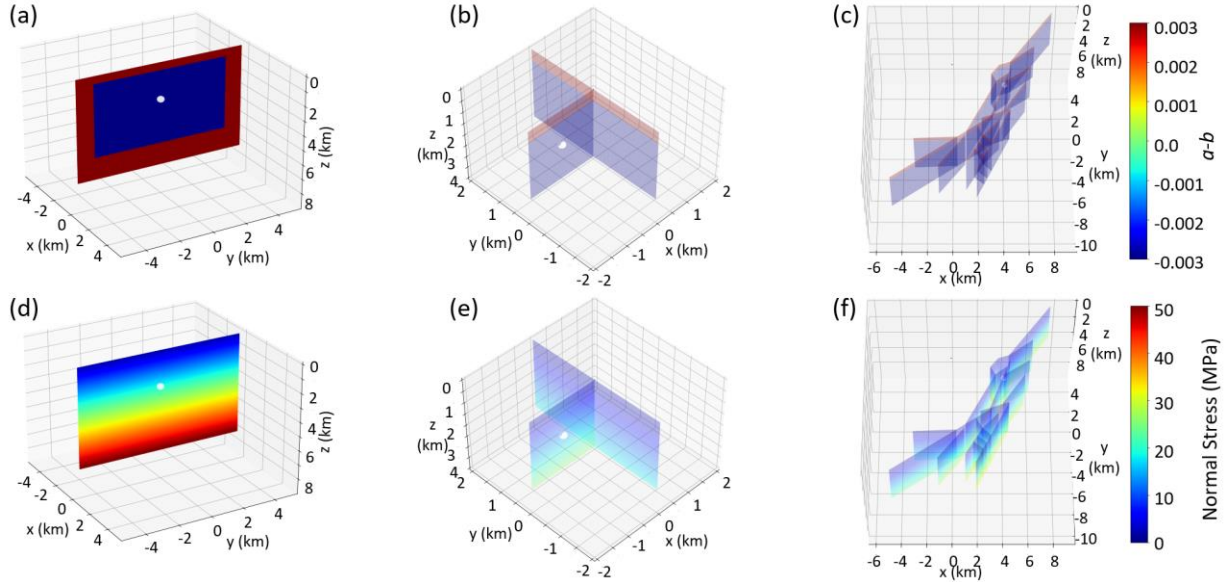
721

722

723

724 **Figures**

725

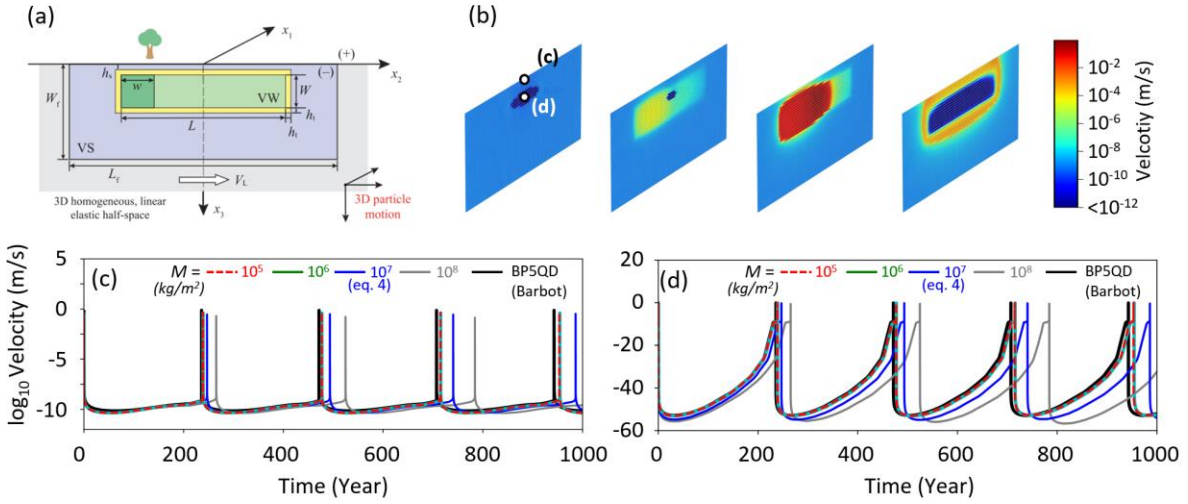


726

727 **Figure 1.** Fault geometries with distributions of friction parameter $a-b$ (a-c) and normal stress (d-
728 f) considered in the simulations of injection-induced seismicity presented in this study. The white
729 sphere denotes the injection location. **(a,d):** Single vertical planar fault. **(b,e):** Branching faults
730 for a 90° angle; simulations for a 60° degree angle were also conducted. **(c,f):** A complex fault
731 system with geometry adopted from the 2012 Prague earthquake, Oklahoma. The normal stress
732 is assumed to increase linearly with depth. Different values of the stress gradient were also
733 tested.

734

735

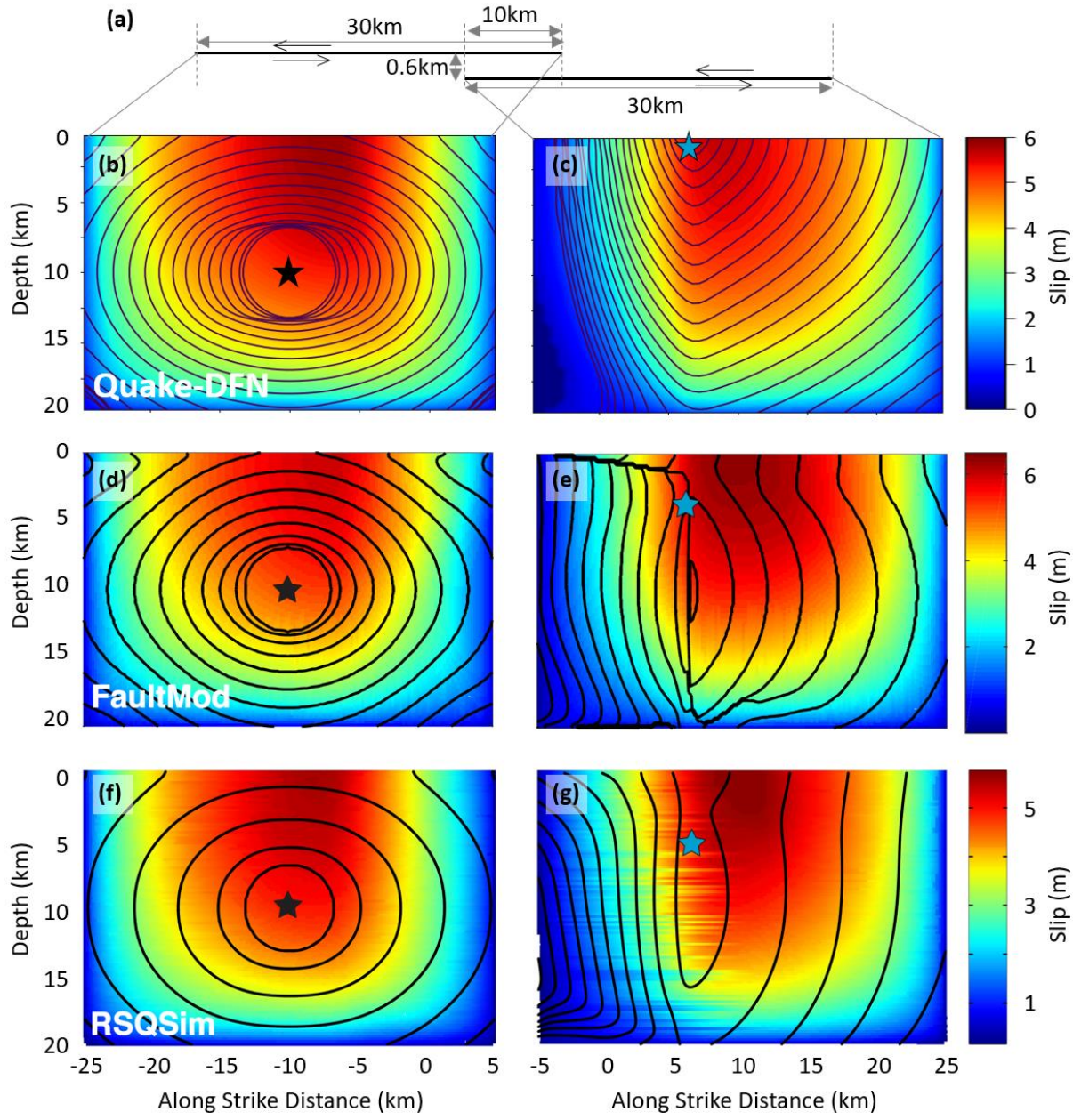


736

737 **Figure 2.** Comparison study #1 for a planar fault (a): Setup of SEAS project benchmark test
 738 BP5-QD [Jiang et al., 2022]. (b): Snapshots of slip rate distribution in our simulation for
 739 $M=10^5 \text{kg/m}^2$. (c,d): Evolution of the slip rate at two points (see panel b for their location) for
 740 comparison of the benchmark simulation (red dashed line) with our simulation result (with $M =$
 741 10^5 (red dashed), 10^6 (green), 10^7 (blue), and 10^8 kg/m^2 (gray). We selected the benchmark
 742 simulation run with Unicycle (Barbot, 2019; black line), which is available on the SEAS project
 743 website. Note that the red dashed and green lines are completely overlapping.

744

745



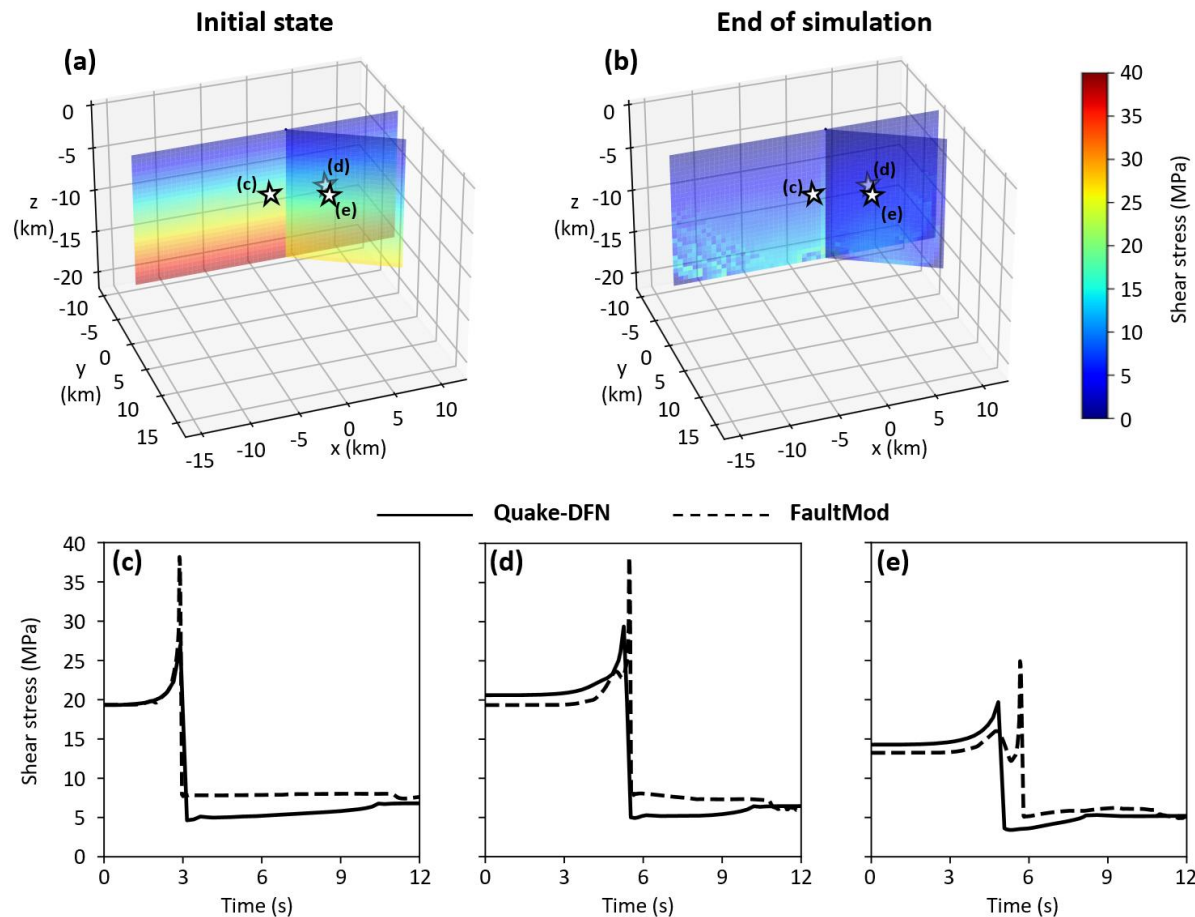
746

747 **Figure 3.** Comparison study #2: Fault step-over. **(a):** fault configuration. **(b-g):** simulation
 748 results of Quake-DFN (b,c), FaultMod (d,e), and RSQSim (f,g). The colored map denotes slip
 749 distribution at the end of the rupture sequence, and the black curves represent rupture contour
 750 every 0.5 s. Rupture is forced nucleated at the black star. The blue stars denote the nucleation
 751 point in the receiver fault. Panels d-g are adopted from Kroll et al. (2023). Note that the color
 752 scales for these panels are slightly different.

753

754

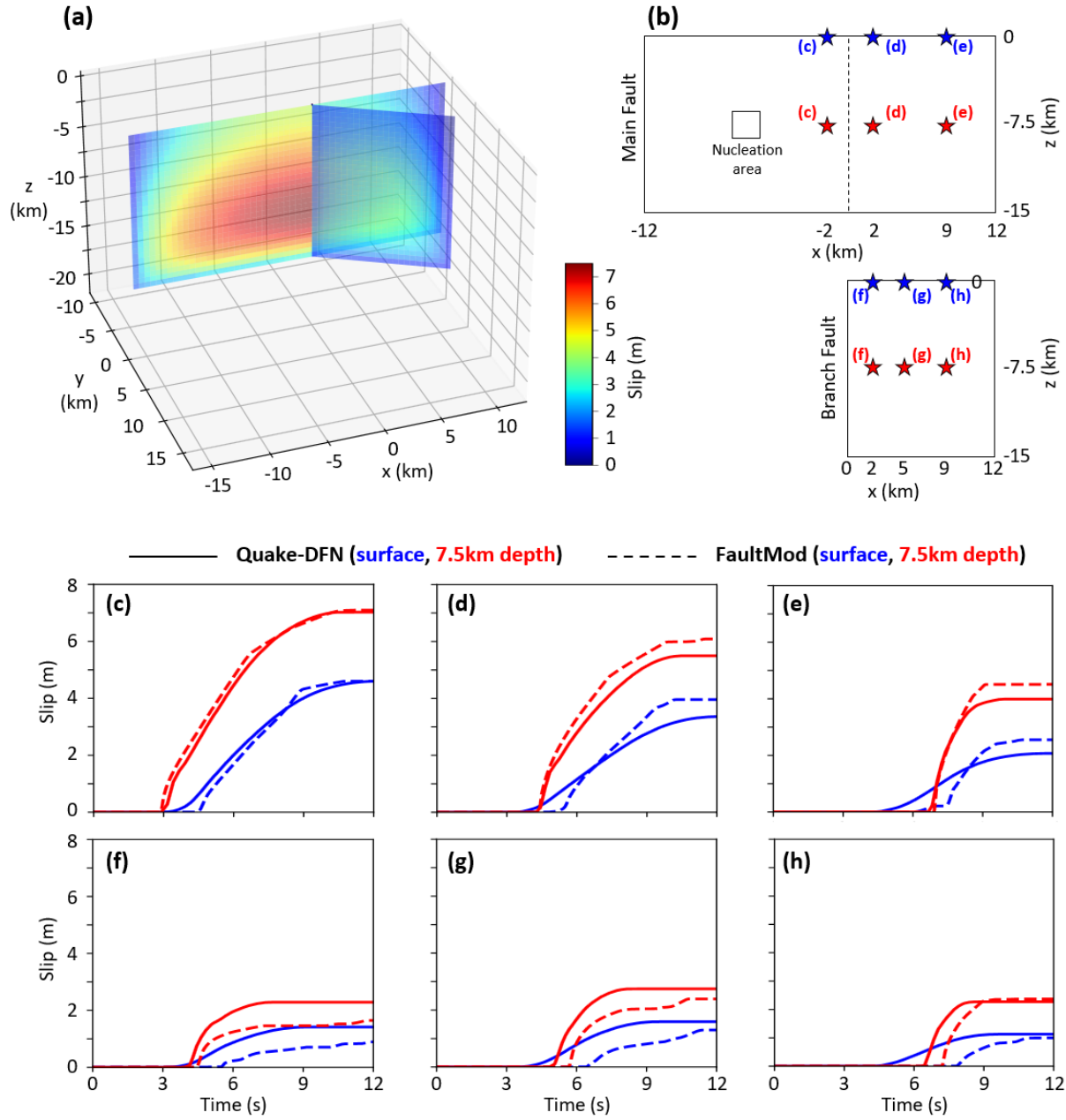
755



756

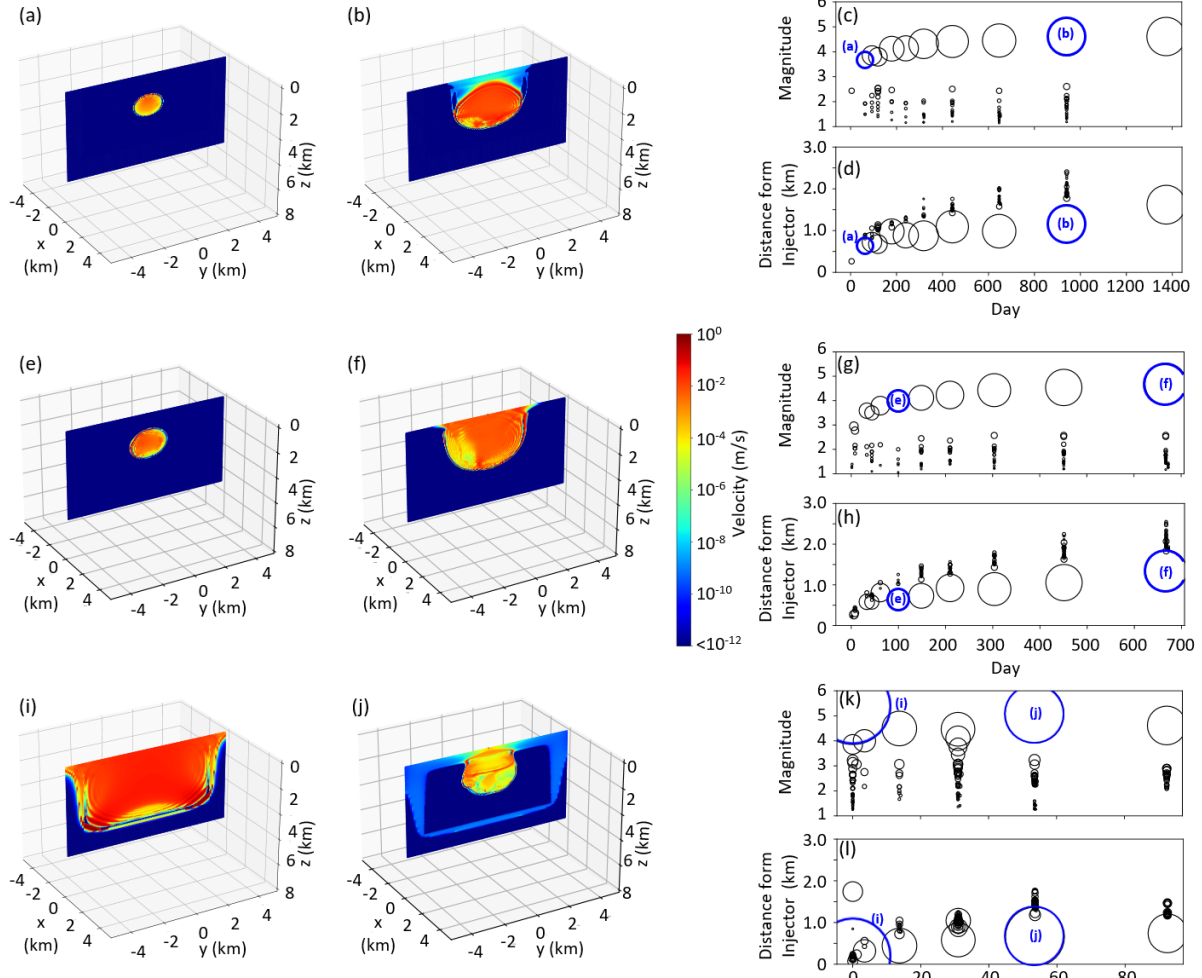
757 **Figure 4.** Comparison study #3, stress changes. (a,b): initial (a) and final (b) shear stress. Initial
 758 stress is depth-dependent for both faults, with the branch fault having lower initial stress. (c-e)
 759 shear stress vs. time at each location denoted in panel (a,b). The time of Quake-DFN result is
 760 shifted by 453 s due to the longer nucleation time, a feature that results from assuming rate and
 761 state friction in Quake-DFN instead of a slip weakening friction in Fault Mod.

762



764 **Figure 5.** Comparison study #3, fault slip. (a) map of fault slip of our simulation result. (b) the
 765 location of the time plot shown in (c-h). Fault slip vs. time for each location indicated in panel
 766 (b). Solid and dashed lines denote our simulation result and FaultMod simulation result,
 767 respectively. The time of Quake-DFN result is shifted for 453s due to the longer nucleation time.

768



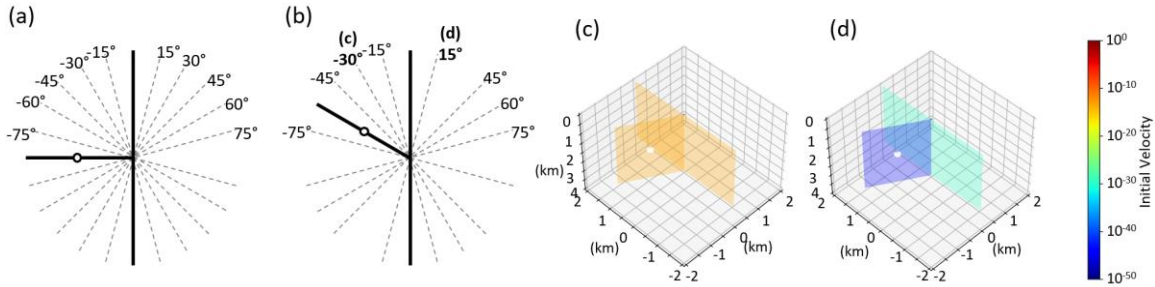
769

770 **Figure 6.** Simulation of earthquakes induced by a fluid injection into a planar fault. **(a-d):**
 771 Simulation result with $V_i = 10^{-30}$ and $\theta_i = 10^6$ s. **(a-d):** Simulation result with $V_i = 10^{-20}$ and $\theta_i =$
 772 10^3 s **(e-h):** simulation results with $V_i = 10^{-15}$ and $\theta_i = 10^9$ s. **(a,b,e,f):** snapshots of slip velocity
 773 during particular events. **(c,g,i):** magnitude vs. time. **(d,h,l):** distance from injector vs. time. The
 774 events corresponding to each snapshot are labeled in the time series plot.

775

776

777



778

779 **Figure 7.** Simulation set up for two interacting faults. **(a,b):** fault orientation (bold lines) and
 780 maximum stress orientation tested (dashed lines) for an angle between the two faults of 90° (a)
 781 and 60° (b). White circles denote injector locations. **(c,d):** Initial velocities of fault angle 60°
 782 with $\mu_0 = 0.4$, $\theta_i = 10^8$ s and maximum stress -30° (c) and 15° (d) (angles shown in (b)).

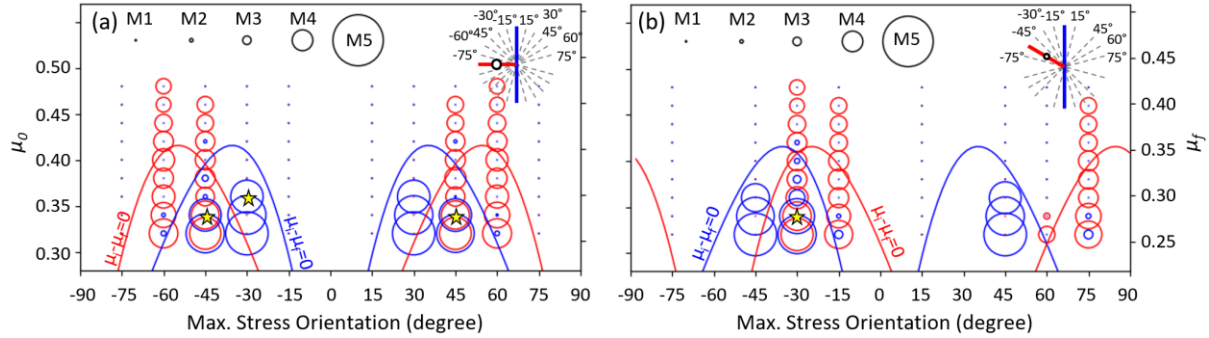
783

784

785

786

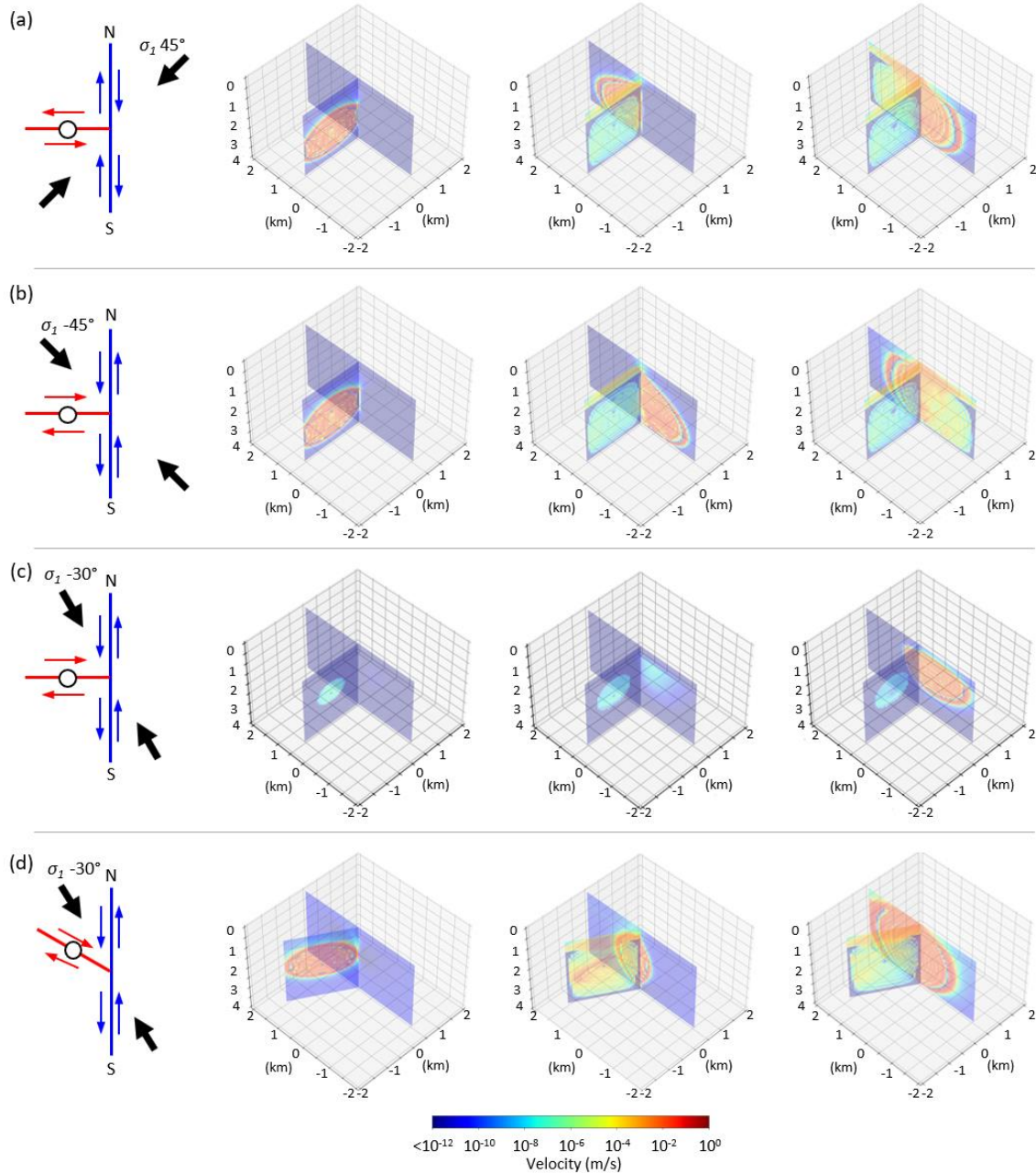
787



788

789 **Figure 8.** Maximum magnitude on the main fault (blue) and the branch fault (red) within one
 790 year for an angle between the two faults of 90° (a) and 60° (b). The simulation setup (detailed in
 791 Figure 7) and the location of the injection are recalled in the inset of each panel. Blue circles
 792 denote events on the main fault, and red circles denote events on the branch fault where the
 793 injection takes place. The rupture sequences for selected cases (yellow stars) are shown in figure
 794 9. The moments are calculated separately for each fault even in the case where both faults are
 795 ruptured simultaneously. Red and blue curves denote the contour line of $\mu_i - \mu_f = 0$ for branch and
 796 main faults, respectively.

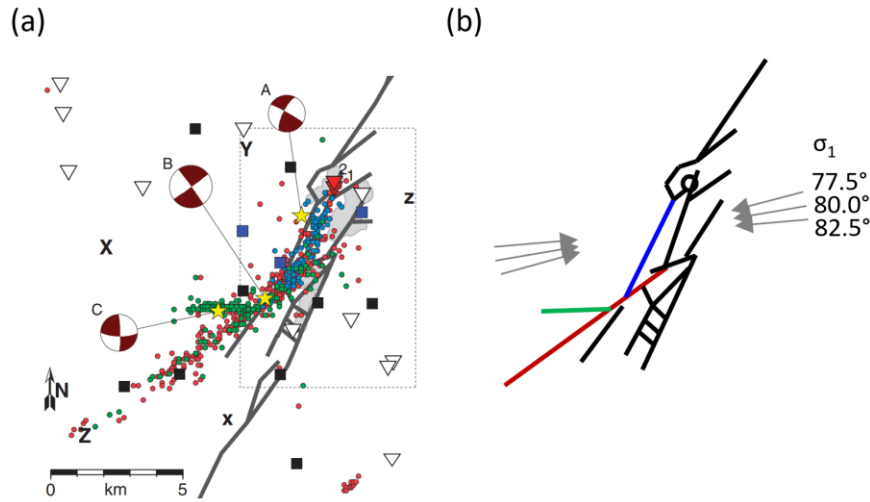
797



798

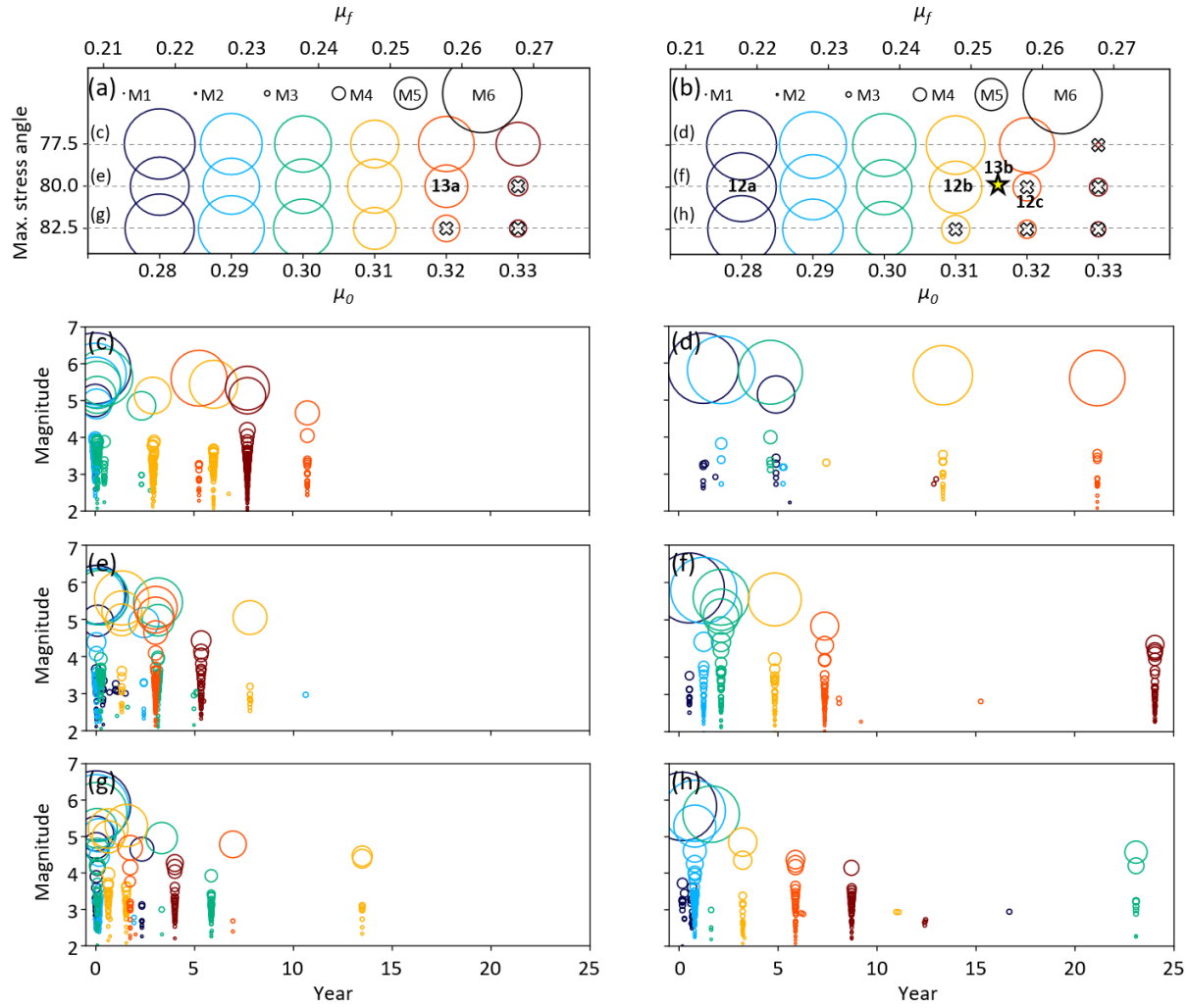
799 **Figure 9.** Snapshots of slip velocity during seismic ruptures induced by a
800 branch faults system. Fault geometry and maximum stress orientation of each setup are shown on
801 the left and in figure 8 (yellow star). In all cases, slip is initiated on the branch fault (red) by the
802 fluid injection, and can be seismic or aseismic, and triggers a fault rupture on the main fault
803 (blue).

804



805 **Figure 10.** Fault geometry for Prague earthquake sequence simulation. (a): Wilzetta faults map
 806 used for reference with focal mechanisms of the M5.0 foreshock (A), M5.7 mainshock (B), and
 807 M5.0 aftershock faults (C) (figure from Keranen et al., 2013). (b): The fault map used for the
 808 simulation. Blue, red, and green faults were activated by the M5.0 foreshock, M5.7 mainshock,
 809 and M5.0 aftershock faults, respectively. The faults ruptured during the mainshock and
 810 aftershock faults were not mapped in the original map. Gray arrows denote three maximum
 811 stress orientations tested in this work.

812



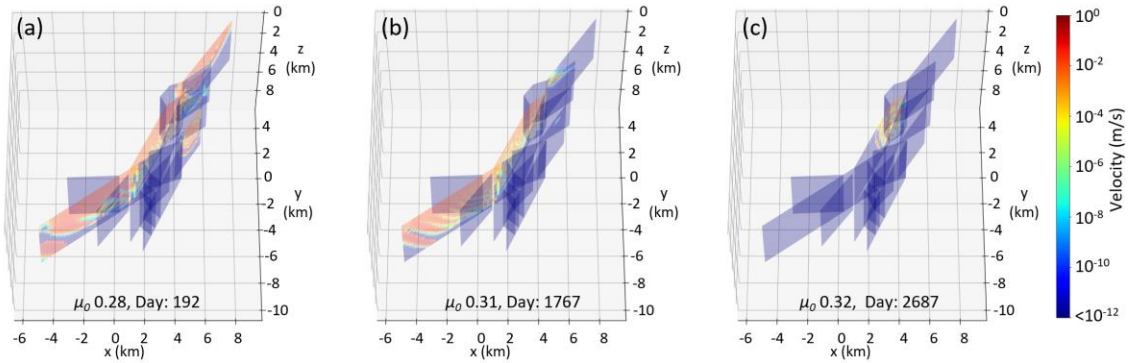
813

814 **Figure 11.** Simulation results for the Wizetta faults system. **(a, b):** maximum
 815 earthquake magnitude within 25 years with $\theta_i = 10^{10}$ s (~ 300 years; panel a) and $\theta_i = 10^{12}$ s ($\sim 30k$ years; panel
 816 b). The X marks denote that the mainshock fault of the Prague earthquake (i.e., the red fault in
 817 figure 9b) did not rupture. **(c, h):** Time series of induced earthquakes.

818

819

820



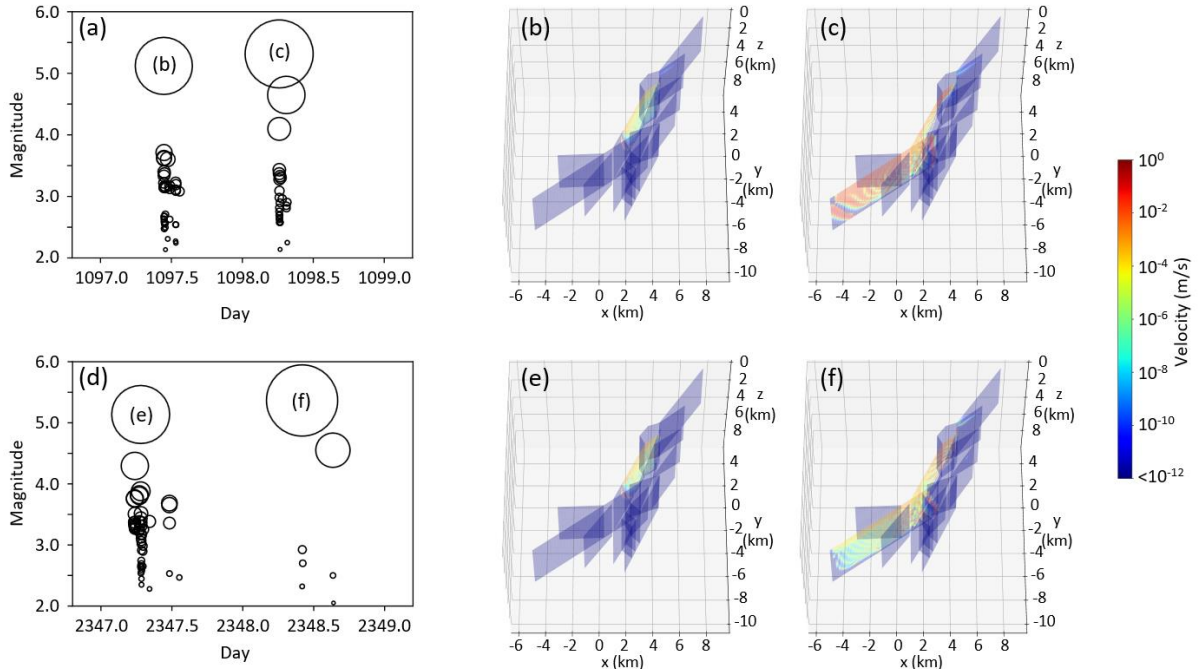
821

822 **Figure 12.** Snapshots of induced earthquakes. The parameter set for each simulation is presented
 823 in figure 11b.

824

825

826



827

828 **Figure 13.** Simulated 1-day delayed rupture. The parameter set for each simulation is presented
 829 in figure 11a and b. **(a,d):** seismicity plot of foreshock and mainshock. **(b,e):** snapshots of
 830 foreshocks. **(c,f):** snapshots of delayed mainshocks.

831

832

833